ELSEVIER

Surface Science 367 (1996) 87–95

surface science

A scanning probe microscopy study of the (001) surfaces of V_2O_5 and V_6O_{13}

Richard L. Smith [a], Gregory S. Rohrer [a,*], K.S. Lee [b], D.-K. Seo [b], M.-H. Whangbo [b]

[a] *Department of Materials Science and Engineering, Carnegie Mellon University, Pittsburgh, PA 15213-3890, USA*
[b] *Department of Chemistry, North Carolina State University, Raleigh, NC 27695-8204, USA*

Received 6 February 1996; accepted for publication 14 May 1996

Abstract

Single crystals of $V_2O_5(001)$ and $V_6O_{13}(001)$ were imaged in ambient conditions by scanning tunneling microscopy (STM) and atomic force microscopy (AFM). Atomic-scale resolution images are compared with partial and total electron-density plots of the surface calculated using the extended Hückel tight-binding electronic band-structure method. The $V_2O_5(001)$ surface is terminated by vanadyl O atoms that dominate the contrast in both AFM and STM images. The $V_6O_{13}(001)$ surface, on the other hand, is terminated by a V–O plane and the contrast in both AFM and STM images is dominated by the V atoms.

Keywords: Atomic Force Microscopy; Scanning Tunneling Microscopy; Surface Structure; Vanadium oxide

1. Introduction

The development of a mechanistic understanding of the chemical processes that occur on transition-metal oxide surfaces requires detailed structural information. Data accumulated over several decades through the application of conventional surface analytical methods is now being complemented by a rapidly expanding body of atomic-scale resolution microscopic observations [1]. For example, the scanning tunneling microscope (STM) has been used to acquire real-space structural data for cuprates [2–11], tungstates [12–15], titanates [16–28], molybdates [29–33], ferrites [34–37] and vanadates [38–40], under a variety of conditions ranging from ultra-high vacuum to ambient. In most of the cases cited above, observations have been interpreted by assuming that filled-state images show the more electronegative atoms, and empty-state images the more electropositive atoms. Unfortunately, this qualitative argument often leaves ambiguities regarding the composition of the termination layer and the relative positions of surface atoms.

It is possible to limit such ambiguities by comparing experimental scanning probe microscopy images with calculated plots of the partial and total surface electron-density. When the tip-sample force interaction is negligible, the STM image of a sample surface is described by the partial electron density plot $\rho(r_0,e_f)$ of the surface [41]. In contact-mode AFM measurements, all the electrons of the surface atoms are involved in repulsive interactions with the tip, so that the AFM image of a sample

* Corresponding author. Fax: +1 412 2687596;
e-mail: gr20@andrew.cmu.edu;
www: http://neon.mems.cmu.edu/rohrer.html

PII S0039-6028(96)00858-8

surface is described by the total electron density plot $\rho(r_0)$ of the surface [42,43]. Such partial and total electron-density plots, calculated using the extended Hückel tight-binding (EHTB) electronic band-structure method [44], have been indispensable in interpreting the observed STM and AFM images of a large number of organic conducting salts, transition-metal chalcogenides and transition-metal halides [42,43]. In the present paper, we use the same method to interpret the STM and AFM images of two related transition-metal oxide surfaces, $V_2O_5(001)$ and $V_6O_{13}(001)$.

2. Crystal and surface structures

2.1. Bulk crystal structures

Both the V_2O_5 and V_6O_{13} structures can be described as being composed of VO_6 octahedra that share corners and edges (Fig. 1a and 1b). Joining the octahedra by sharing corners along one dimension creates a chain with the stoichiometry VO_5, and linking two such chains by corners creates a V_2O_9 double octahedral chain. The idealized V_2O_5 structure [45] is obtained from the V_2O_9 double chains first by sharing their edges to form a V_4O_{14} layer, and then by sharing the apical oxygen atoms of adjacent parallel V_4O_{14} layers to form the V_4O_{10} structure (Fig. 1a). The V_6O_{13} structure is derived from this arrangement by a crystallographic shear operation of $1/2\langle 101\rangle$ on every other V_4O_{14} layer, so that the adjacent layers become joined by edge-sharing (Fig. 1b). In projection along [001], V_2O_5 and V_6O_{13} have a similar polyhedral connectivity and a similar two-dimensional repeat unit; the unit cell of the $V_2O_5(001)$ surface is 11.52 Å × 3.56 Å, and that of the $V_6O_{13}(001)$ surface is 11.92 Å × 3.68 Å. It is this similarity that makes a comparison of their surface images interesting.

To understand the differences between V_2O_5 and V_6O_{13}, it is important to note that their VO_6 octahedra are not regular [46,47]. The V coordination in V_2O_5 is best described as square pyramidal because the VO_6 octahedra of every V_4O_{14} layer have alternately strong and weak bonds, O–V···O, along [001] (V–O = 1.58 Å and V···O = 2.78 Å), and the V···O distance should be considered a van der Waals contact [48]. Within each V_2O_9 double chain of a V_4O_{14} layer, the direction of the O–V–O bond alternation is the same. Between adjacent V_2O_9 double chains of a V_4O_{14} layer, however, the directions of their O–V···O bond alternations are opposite. Thus, the V_4O_{10} structure consists of isolated layers of composition V_4O_{10} parallel to (001), and these layers are held together by the van der Waals V···O bonds. In V_6O_{13}, on the other hand, the V–O bonding is more isotropic. The longest V–O bonds in the corner-sharing layers parallel to (001) are 1.99 Å, and those in the edge-sharing layers are 2.27 Å.

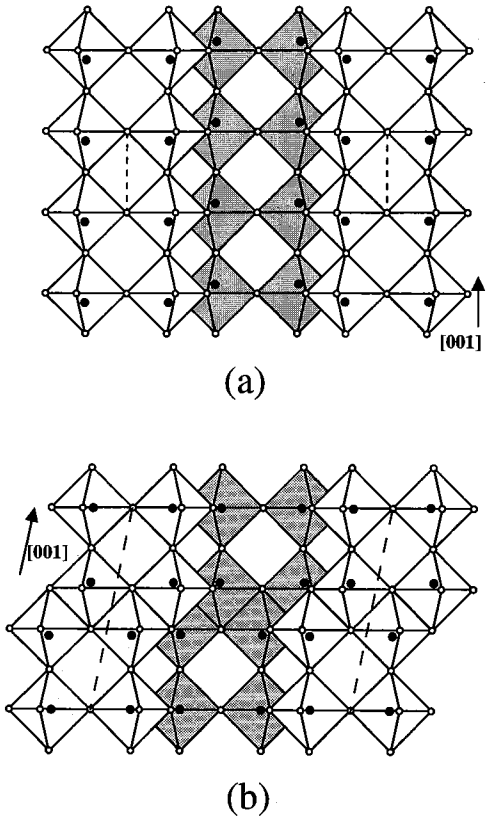

Fig. 1. Idealized polyhedral representations comparing the structures of (a) V_2O_5 and (b) V_6O_{13}. To emphasize the topological similarity of the two structures, it is assumed that the V atoms are in regular octahedral coordination. Both structures are projected along [010]. Shaded polyhedra are in a plane behind the unshaded ones, and the dashed lines mark the boundaries of the unit cell.

This structural difference between V_2O_5 and V_6O_{13} is manifest in their mechanical properties. V_2O_5 is micaceous and can be cleaved with adhesive tape, while V_6O_{13} is more robust and must be cleaved with a razor blade.

2.2. Surface structures

Possible surface structures of V_2O_5 and V_6O_{13} can be classified on the basis of the V–O bonds perpendicular to the (001) cleavage planes. When V_2O_5 is cleaved parallel to (001), the van der Waals V···O contacts between the adjacent V_4O_{10} layers will be broken to create two identical surfaces (Fig. 2a). A projected view of this surface is shown in Fig. 3a.

The termination pattern on cleaved $V_6O_{13}(001)$ surfaces cannot be specified with the same degree of certainty. A projected view of the $V_{12}O_{30}$ slab, which represents the three consecutive V_4O_{14} layers that make up the V_6O_{13} structure (i.e. two edge-shared and one corner-shared) is shown in Fig. 2b. Cleavage parallel to (001) involves breaking axial V–O bonds (i.e. those roughly perpendicular to (001)), and Fig. 2b shows three possible cleavage planes (A–C). Cleavage at plane B breaks the shortest V–O bonds (1.64–1.66 Å). The bonds broken when the structure cleaves at plane A are somewhat longer (1.96–1.99 Å), and the bonds that must be broken along C are the longest (about 2.27 Å). However, the density of bonds in plane C is double that in plane A or B. Assuming that the longest bonds will break, cleavage is most likely to occur at plane A or C.

Plane A and B differ from plane C in two important ways that allow them to be distinguished experimentally. First, there are two A and B planes in each repeat unit, but only one C plane. Thus, cleavage on the A or B planes could lead to surface steps with heights that are not integer multiples of the unit-cell size. Cleavage on the C plane, however,

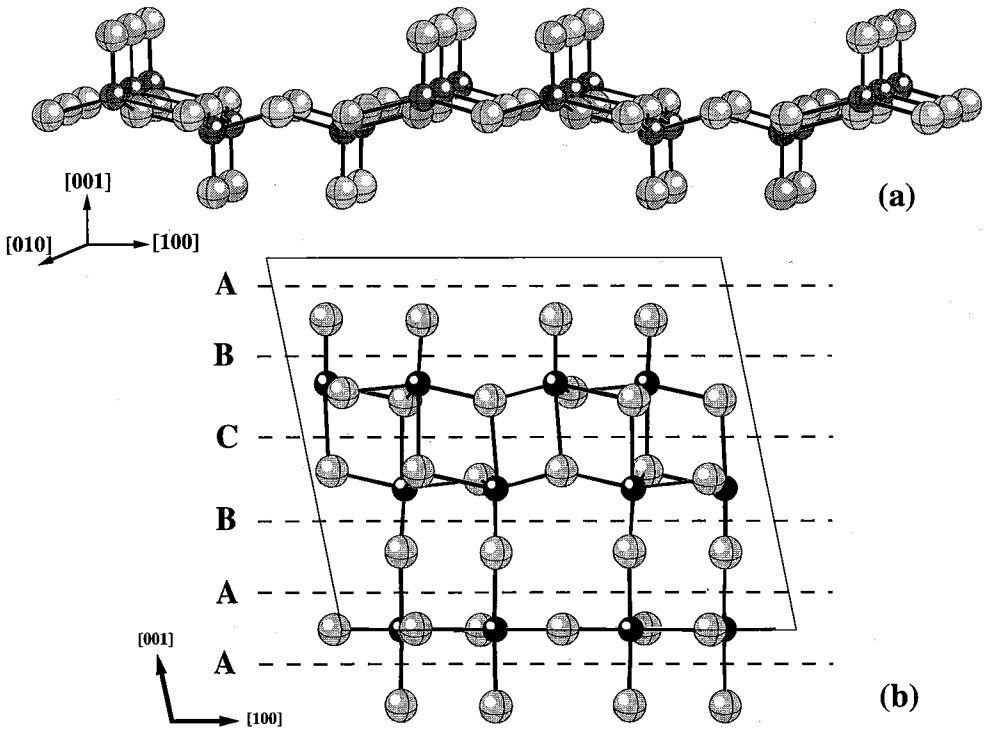

Fig. 2. (a) Perspective view of the V_4O_{10} layer of V_2O_5. (b) Projected view of the $V_{12}O_{30}$ slab, representing three consecutive octahedral layers of the V_6O_{13} structure terminated by oxygen atoms on both surfaces. The labels A, B and C are three possible cleavage planes of V_6O_{13} leading to surfaces parallel to (001).

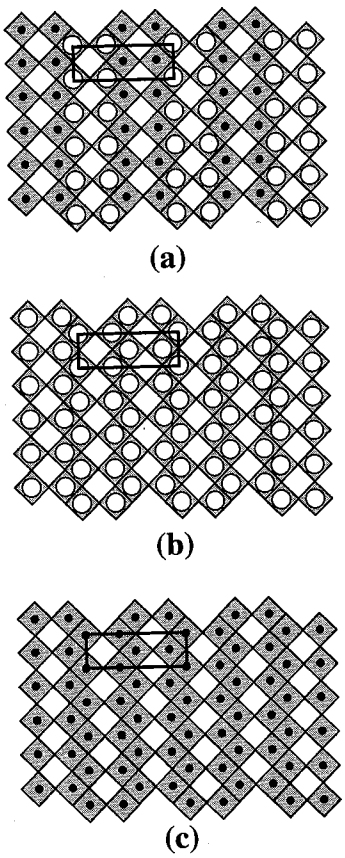

Fig. 3. Schematic [001] projection views of the surfaces of (a) V_2O_5, (b) oxygen-terminated surface of V_6O_{13} surface (surface 1), and (c) V/O-terminated surface of V_6O_{13} (surface 2). The shaded diamonds represent the projections of the V/O polyhedra. A large white circle represents a capping apical oxygen, and a small black circle an uncapped V atom.

can only yield steps that are integer multiples of the unit-cell height. The second difference is that cleavage at A or B must simultaneously create two surfaces with different compositions, while cleavage at C creates only one type of surface. For example, cleaving the bonds in the A plane creates one surface terminated by the apical O atoms of the short V–O bonds of the edge-sharing V_4O_{14} layer (surface 1) and another that is terminated by the V and basal O atoms of the corner-sharing V_4O_{14} layer (surface 2). Schematic projections of each of the surfaces are shown in Figs. 3b and 3c, respectively. Cleavage at plane C, on the other hand, creates two identical surfaces that are both terminated by the V and basal O atoms (surface 3). In projection along [001], surface 3 is similar to surface 2 (Fig. 3c).

To simulate the electronic structure of the $V_2O_5(001)$ surface, EHTB calculations were carried out on an isolated V_4O_{10} layer. The $V_{12}O_{30}$ slab was used to calculate the electronic structure of surface 1 (Fig. 3b) and the electronic structure of surface 2 was calculated using the $V_{12}O_{26}$ slab, which is derived from the $V_{12}O_{30}$ slab by removing the apical oxygen atoms (on the lower part of Fig. 2b). Likewise, the electronic structure of surface 3 can be simulated using the V_8O_{20} slab, which is generated from the $V_{12}O_{30}$ slab by cleaving at plane C. In each case, atoms are assumed to occupy their bulk positions and the effects of relaxation are ignored.

3. Experimental procedure

Brown, lustrous crystals of $Na_{0.003}V_2O_5$ were grown by transporting $Na_xV_2O_5$ powder with $TeCl_4$ in a small temperature gradient near 530°C [40]. Black, platy crystals of V_6O_{13} were grown by transporting stoichiometric mixtures of V_2O_5 and V_2O_3 powders with $TeCl_4$ in a small temperature gradient around 600°C [49]. In each case, the identity of the phase and the orientation of the crystal were established using conventional X-ray diffraction methods. Based on a least-squares refinement of the peak positions in the powder diffraction patterns, the lattice parameters of V_2O_5 were $a=11.4959(95)$ Å, $b=3.5510(51)$ Å and $c=4.3569(25)$ Å, and the lattice parameters of V_6O_{13} were $a=11.92(1)$ Å, $b=3.680(2)$ Å, $c=10.14(1)$ Å and $\beta=101.0(2)°$. These measurements are consistent with the established parameters. Because pure V_2O_5 is too insulating for STM experiments, it was donor-doped with Na which intercalates and occupies positions in the van der Waals gap. V_6O_{13} is a mixed-valence compound and is conductive without doping. Four-probe electrical resistivity measurements show that the conductivity of the Na-doped V_2O_5 is 25 $\Omega\cdot$cm, and that of V_6O_{13} is 0.014 $\Omega\cdot$cm. Each crystal is easily cleaved to expose (001) facets that are stable during both STM and AFM analysis in air.

Topographic STM images were recorded in air with mechanically clipped Pt–Ir tips and constant currents of 0.5–1.0 nA. Images of V_2O_5 could be recorded at a range of positive and negative sample biases and showed the same essential features. The highest resolution image, shown in Fig. 4a, was recorded using a sample bias of −0.54 V. Images of V_6O_{13}, recorded at biases between −0.6 and 0.6 V, also showed no noticeable bias dependence. The highest-resolution image, shown in Fig. 4c, was recorded using a sample bias of −0.6 V. Both of these crystals are *n*-type and the Fermi level is near the bottom of the conduction band, which is separated from the top of the valence band by a gap of more than 2 eV. Therefore, all the images were recorded by tunneling to or from states near the bottom of the conduction band. Because similar energy levels are sampled in both polarities, the bias independence of the contrast is not too surprising. Topographic AFM images were recorded with pyramidal Si_3N_4 tips and constant forces of 0.75–8 nN. Thermal drift affects all of the data to a greater or lesser degree and can be corrected based on observations recorded while scanning in different directions. The thermal drift was subtracted from only one of the images presented here (Fig. 4d). The atomic-scale resolution images presented here are representative of many observations on multiple crystals and are small subsets of images selected from defect-free regions of the surface. After subtracting a background plane to remove specimen tilt, the images were Fourier-filtered to remove random noise. This procedure is used to clarify the features that are apparent in the raw data.

4. STM and AFM results

4.1. Image contrast

A 21 Å × 21 Å STM image of the $V_2O_5(001)$ surface is shown in Fig. 4a. The dominant contrast features are the pairs of round white spots that

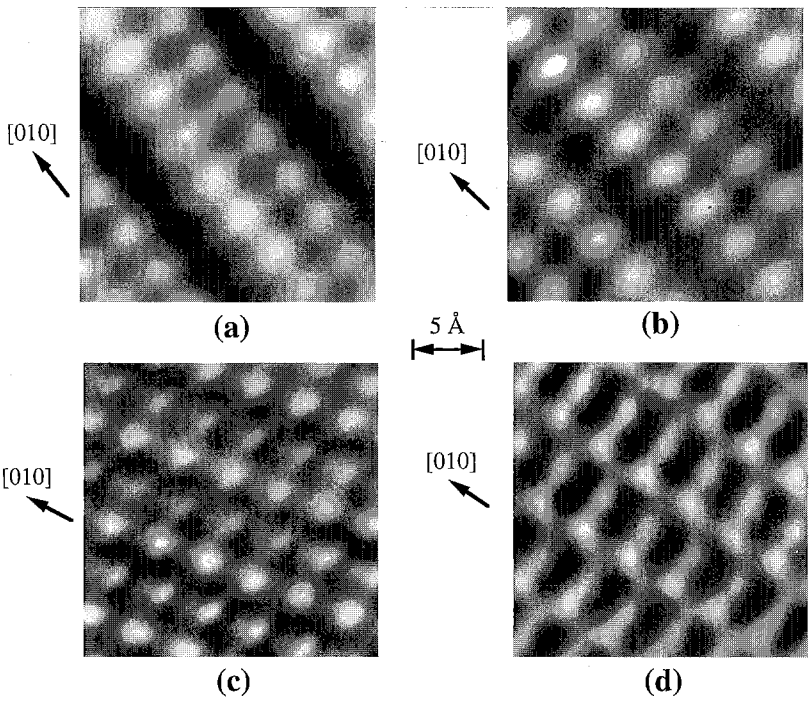

Fig. 4. (a) 21 Å × 21 Å STM image of the $V_2O_5(001)$ surface. (b) 21 Å × 21 Å AFM image of the $V_2O_5(001)$ surface. (c) 21 Å × 21 Å STM image of the $V_6O_{13}(001)$ surface. (d) 21 Å × 21 Å AFM image of the $V_6O_{13}(001)$ surface.

form rows along the [010] axis. The corrugations over these positions are approximately 0.55 Å along [100] and 0.3 Å along [010]. The features form a rectangular repeat unit, which is equal in dimension to the unit cell of the $V_2O_5(001)$ surface, i.e. 11.5 Å × 3.56 Å. The small differences in the brightness of the different spots in the pattern represent topographic height differences of the order of 0.1 Å, and were not observed reproducibly. The contrast in contact AFM images of this surface is similar, as shown in Fig. 4b. One difference is that the topographic corrugations over the features are small (of the order of 0.1 Å). Larger corrugations can be measured at higher force set points, but the larger force settings also cause increased thermal drift. A 21 Å × 21 Å STM image of the $V_6O_{13}(001)$ surface is shown in Fig. 4c. Again, the dominant contrast features are the pairs of white spots. However, in this case, they are arranged to form a centered rectangular cell with the unit-cell dimensions of the $V_6O_{13}(001)$ surface. It is also important to note that the spots are always elongated along [010] and, in some cases, are split into two separate contrast peaks. The vertical corrugations over these features are about 1 Å. In the AFM images of the $V_6O_{13}(001)$ surface (Fig. 4d), a similar centered rectangular repeat unit with the unit-cell dimensions of the $V_6O_{13}(001)$ surface is easily identified. The contrast consists of staggered white rows along [010], in which two separate contrast peaks can sometimes be resolved. Each of the images shown in Fig. 4 is characteristic of all our observations in defect-free regions of the crystal, and we therefore conclude that only one type of surface termination was imaged.

4.2. Step heights

To distinguish between the possible termination models for V_6O_{13} that were discussed in Section 2.2, we measured the distribution of step heights on the cleaved surfaces. The AFM image in Fig. 5 shows the typical surface topography. Cleaved surfaces are characterized by terraces that terminate in sharp points. The heights of 121 steps, selected from several dozen images similar to the one shown in Fig. 5, were measured using the topographic data. All of the topographic profiles

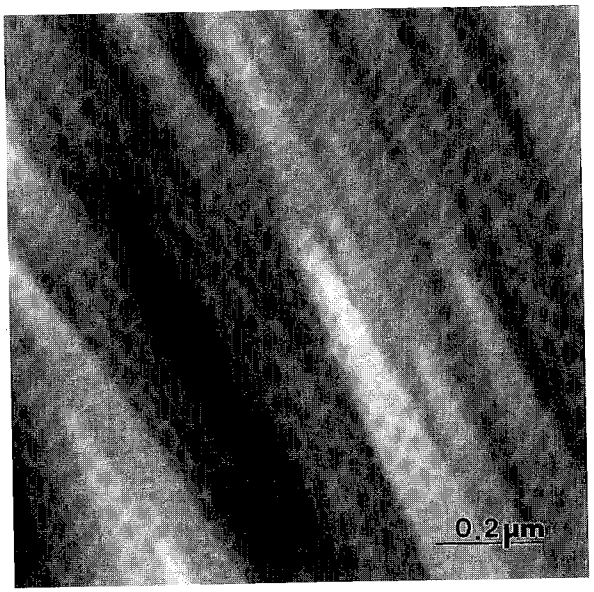

Fig. 5. AFM image showing a 1.1 μm × 1.1 μm area of the $V_6O_{13}(001)$ surface. The adjacent flat terraces in this image are separated by steps that are approximately 10 Å high.

for the height measurements were taken from single scan lines in which flat terraces could be distinguished on either side of the step. The distribution of the 98 smallest steps (Fig. 6) is sharply peaked, with the mean value at 10.8 ± 0.56 Å, and 97% of all the measurements fall within two standard deviations of the mean. The measured step height

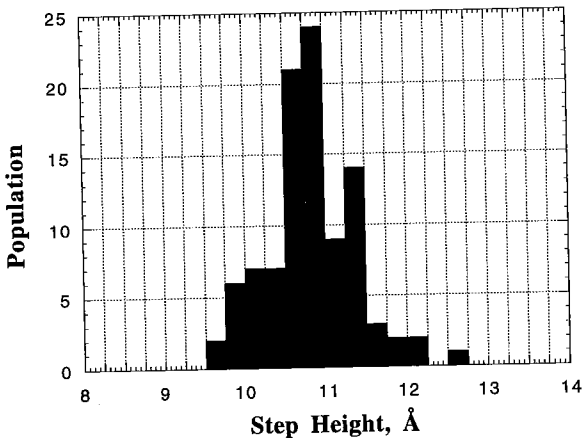

Fig. 6. Heights of 98 steps between terraces on the cleaved $V_6O_{13}(001)$ surface. The mean value of the distribution is 10.8 Å with a standard deviation of 0.56 Å.

of 10.8 Å can be assigned to the height of a single unit cell, which should be 10.0 Å (height $= c \sin \beta$). We assume that the small difference is due to an error in the piezo calibration. The remaining 23 steps that are not part of the distribution peaked at 10.8 Å are narrowly distributed around 21.6 Å. The smallest possible sub-unit cell step would be about 2 Å high. Because no 2 Å steps are observed, and because there are no peaks at ± 2Å of the mean value 10.8 Å, it is concluded that all the steps formed during cleavage are integer multiples of the unit-cell height.

5. Density plot calculations and image analysis

The $\rho(r_0,e_f)$ and $\rho(r_0)$ plots calculated for an isolated V_4O_{10} layer are presented in Figs. 7a and 7b, respectively. The high electron-density (HED) spots of the two plots are all located at the apical oxygen atoms (i.e. the atoms protruding farthest from the surface). The HED spots are arranged in the same pattern as the bright spots in the STM/AFM images (Figs. 4a and 4b), and we therefore conclude that the white spots on the STM and AFM images are the apical O atoms. As was observed during STM imaging experiments, the essential features of the pattern are the same when states on either side of the Fermi level are sampled.

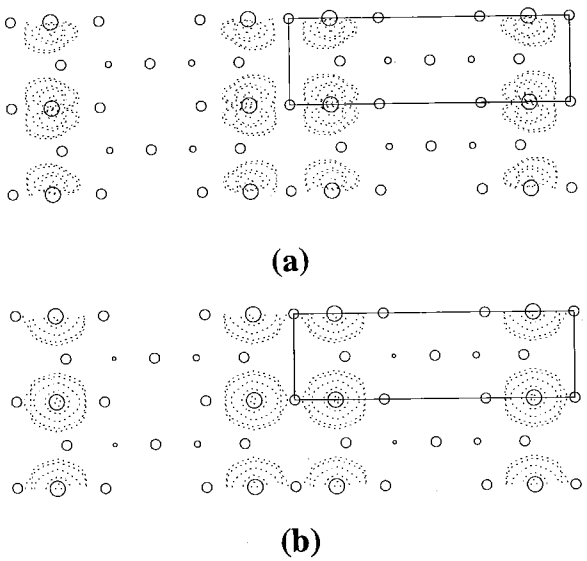

Fig. 7. Partial and total density plots calculated for the $V_2O_5(001)$ surface. (a) $\rho(r_0,e_f)$ plot. The contour values used are 0.3, 0.1, 0.05, 0.01 and 0.005×10^{-3} electrons per au^3. (b) $\rho(r_0)$ plot. The contour values used are 0.5, 0.2, 0.05, 0.01 and 0.005 electrons per au^3.

As described in Section 2.2, several possible (001) surfaces might be revealed when V_6O_{13} is cleaved. The $\rho(r_0,e_f)$ plot calculated for surfaces 1, 2 and 3 are compared in Figs. 8a, 8b and 8c, respectively. The HED spots on surface 1 correspond to the apical O positions. The HED spots on surface 2 and 3, on the other hand, correspond to V positions. While each of the plots shows a centered rectangular arrangement formed by pairs of HED spots, there are details which can be used to distinguish them. For example, the distance between the electron density peaks in each pair of spots aligned along [010] is greatest for surface 2 and smallest for surface 3. The distance between the HED spots on surface 3 is closest to the STM observations. Furthermore, the electron-density contours around the HED peaks on surface 3 are elongated along [010] and have two peaks, as in the STM image, while those in surface 1 and 2 are elongated along [100]. Therefore, based on the positions and shapes of the HED peaks, surface 3, shown in Fig. 8c, is most consistent with the experimental image (Fig. 4c). If this is the correct assignment, then the $\rho(r_0)$ plot calculated for the same surface should be consistent with the AFM image shown in Fig. 4d. In Fig. 8d, we see that the $\rho(r_0)$ plot has round HED spots centered at the V atoms. These spots occur in pairs along [010], as the spots in the experimental image do. One difference is that the relative distance between the electron-density peaks in each pair of spots appears to be smaller in the experimental image than in the $\rho(r_0)$ plot. However, the $\rho(r_0)$ plots for the other surfaces (not shown) do not show better agreement.

All of the data presented above is consistent with the conclusion that V_6O_{13} cleaves at the C plane to reveal surface 3, terminated by V and O atoms. The experimental signatures associated with cleavage at the A or B plane (multiple termination patterns and step heights that are not integer multiples of the unit cell distance) were never observed. Furthermore, when the experimental STM image is compared to calculated $\rho(r_0,e_f)$ plots,

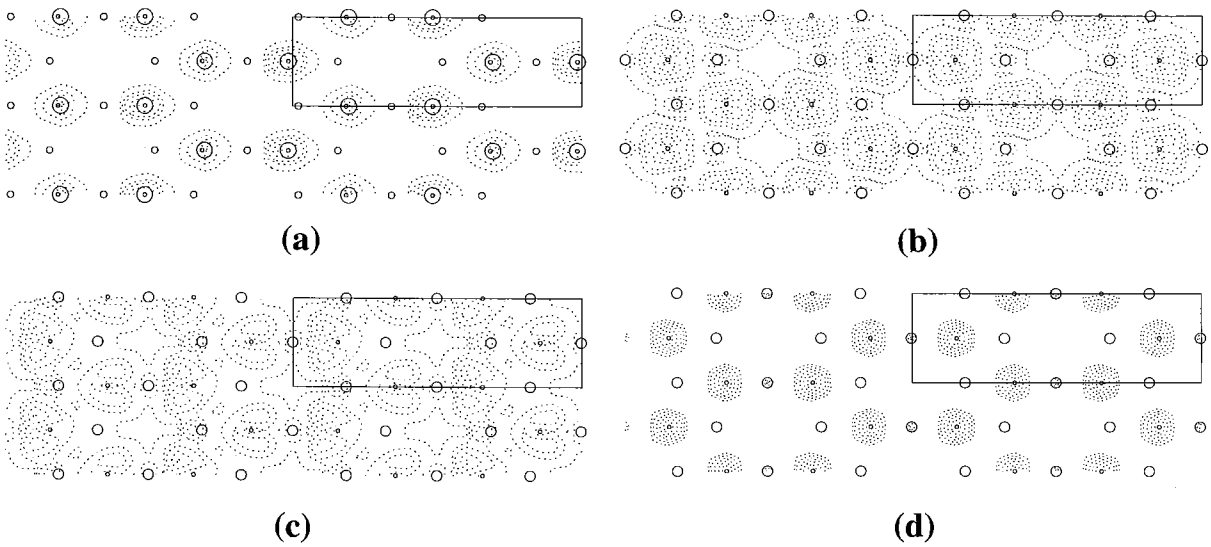

Fig. 8. Partial and total density plots calculated for the $V_6O_{13}(001)$ surface. (a) $\rho(r_0,e_f)$ plot for surface 1. The contour values used are 0.6, 0.5, 0.4, 0.3, 0.2, and 0.1×10^{-3} electron per au^3. (b) $\rho(r_0,e_f)$ plot for surface 2. The contour values used are 0.15, 0.10, 0.05, 0.01, and 0.005×10^{-1} electron/au^3. (c) $\rho(r_0,e_f)$ plot for surface 3. The contour values used are 0.3, 0.2, 0.1, 0.05 and 0.01×10^{-2} electrons per au^3. (d) $\rho(r_0)$ plot for surface 3. The contour values used are 0.4, 0.3, 0.2, 0.1 and 0.05 electrons per au^3.

the electron contours for surface 3 most nearly reproduce the observed image's distinguishing characteristics. Finally, the $\rho(r_0)$ plot for this same surface is consistent with the AFM image.

6. Concluding remarks

By comparing experimental observations to the calculated total and partial electron-density plots, we conclude that the $V_2O_5(001)$ surface is terminated by vanadyl O atoms, and that the $V_6O_{13}(001)$ surface is terminated by a V–O plane. It is interesting to note that while all of the STM images were formed by probing conduction-band states, the HED positions in images of $V_2O_5(001)$ corresponded to O atom positions, while the HED positions in images of $V_6O_{13}(001)$ corresponded to V atom positions. These results can be taken to represent two limiting cases that occur at the surfaces of the many transition-metal oxides which have O anions arranged in a pseudo-octahedral geometry about the metal cation. When the M–O polyhedra are terminated by an apical O that lies at a position more than 1 Å above the metal atom, the O atom dominates the contrast. When the metal and O lie in the same plane, the metal atoms dominate the contrast.

Finally, we note that relaxation apparently plays an insignificant role in determining the structure of these surfaces. All of the electron-density plots were computed based on the assumption that atoms remain in their bulk positions after cleavage. While this is not a valid approximation in the general case, it is acceptable here because only the longest (weakest) bonds in these anisotropic structures were broken, and these surfaces have a low driving force for relaxation.

Acknowledgements

G.S.R. and R.L.S. acknowledge support from the National Science Foundation under YIA Grant DMR-9458005, and thank Dr. P. Marella, Park Scientific Instruments, for technical assistance. The work at North Carolina State University was supported by the US Department of Energy, Office of Basic Sciences, Division of Materials Sciences, under Grant DE-FG05-86ER45259.

References

[1] V.E. Henrich and P.A. Cox, The Surface Science of Metal Oxides (Cambridge University Press, Cambridge, 1994).
[2] M.D. Kirk, J. Nogami, A.A. Baski, D.B. Mitzi, A. Kapitulnik, T.H. Geballe and C.F. Quate, Science 242 (1988) 1674.
[3] M.D. Kirk, C.B. Eom, B. Oh, S.R. Spielman, M.R. Beasley, A. Kapitulnik, T.H. Geballe and C.F. Quate, Appl. Phys. Lett. 52, 2071 (1988).
[4] C.K. Shih, R.M. Feenstra, J.R. Kirtley and G.V. Chandrashekhar, Phys. Rev. B 40 (1989) 2682.
[5] T. Hasegawa and K. Kitazawa, Jpn. J. Appl. Phys. 29 (1990) L434.
[6] X.L. Wu, Z. Zhang, Y.L. Wang and C.M. Lieber, Science 248 (1990) 1211.
[7] C.K. Shih, R.M. Feenstra and G.V. Chandrashekhar, Phys. Rev. B 43 (1990) 7913.
[8] Z. Zhang and C.M. Lieber, J. Phys. Chem. 96 (1992) 2030.
[9] K. Ikeda, K. Takamuku, R. Itti and N. Koshizuka, Surf. Sci. 290 (1993) 207.
[10] M. Kawasaki and M. Nantoh, MRS Bull., Sept. 1994, p. 33.
[11] K. Koguchi, T. Matsumoto and T. Kawai, Science 267 (1995) 71.
[12] M.L. Norton, J.G. Mantovani and R.J. Warmack, J. Vac. Sci. Technol. A 7 (1989) 2898.
[13] W. Lu, N. Nevins, M.L. Norton and G.S. Rohrer, Surf. Sci. 291 (1993) 395.
[14] G.S. Rohrer, W. Lu, M.L. Norton, M.A. Blake and C.L. Rohrer, J. Solid State Chem. 109 (1994) 359.
[15] F.H. Jones, K. Rawlings, S. Parker, J.S. Foord, P.A. Cox, R.G. Egdell and J.B. Pethica, Surf. Sci. 336 (1995) 181.
[16] G.S. Rohrer, V.E. Henrich and D.A. Bonnell, Science 250 (1990) 1239.
[17] G.S. Rohrer, V.E. Henrich and D.A. Bonnell, Surf. Sci. 278 (1992) 146.
[18] P.W. Murray, F.M. Leibsle, H.J. Fisher, C.F.J. Flipse, C.A. Muryn and G. Thornton, Phys. Rev. B 46 (1992) 12877.
[19] M. Sander and T. Engel, Surf. Sci. 302 (1994) L263.
[20] H. Onishi and Y. Iwasawa, Surf. Sci. 313 (1994) L783.
[21] A. Szabo and T. Engel, Surf. Sci. 329 (1995) 241.
[22] P.W. Murray, N.G. Condon and G. Thornton, Phys. Rev. B 51 (1995) 10989.
[23] S. Fischer, A.W. Munz, K-D. Schierbaum and W. Göpel, Surf. Sci. 337 (1995) 17.
[24] T. Matsumoto, H. Tanaka, T. Kawai and S. Kawai, Surf. Sci. 278 (1992) L153.
[25] Y. Liang and D.A. Bonnell, Surf. Sci. 285 (1993) L510.
[26] Y. Liang and D.A. Bonnell, Surf. Sci. 310 (1994) L128.
[27] T. Matsumoto, H. Tanaka, K. Kouguchi, T. Kawai and S. Kawai, Surf. Sci. 312 (1994) 21.
[28] Y. Liang and D.A. Bonnell, J. Am. Ceram. Soc. 78 (1995) 2633.
[29] J. Heil, J. Wesner, B. Lommel, W. Assmus and W. Grill, J. Appl. Phys. 65 (1989) 5220.
[30] E. Garfunkel, G. Rudd, D. Novak, S. Wang, G. Ebert, M. Greenblatt, T. Gustafsson and S.H. Garofallini, Science 246 (1989) 99.
[31] G. Rudd, D. Novak, D. Saulys, R.A. Bartynski, S.H. Garofallini, K.V. Ramanujachary, M. Greenblatt and E. Garfunkel, J. Vac. Sci. Technol. B 9 (1991) 909.
[32] U. Walter, R.E. Thomson, B. Burk, M.F. Crommie, A. Zettl and J. Clarke, Phys. Rev. B 45 (1992) 11474.
[33] G.S. Rohrer, W. Lu, R.L. Smith and A. Hutchinson, Surf. Sci. 292 (1993) 261.
[34] R. Wiesendanger, I.V. Shvets, D. Bürgler, G. Tarrach, H.J. Güntherodt, J.M.D. Coey and S. Gräser, Science 255 (1992) 583.
[35] G. Tarrach, D. Bürgler, T. Schaub, R. Wiesendanger and H.J. Güntherodt, Surf. Sci. 285 (1993) 1.
[36] N.G. Condon, P.W. Murray, F.M. Leibsle, G. Thornton, A.R. Lennie and D.J. Vaughan, Surf. Sci. 310 (1994) L609.
[37] R. Jansen, V.A.M. Brabers and H. van Kempen, Surf. Sci. 328 (1995) 237.
[38] T. Oshio, Y. Sakai, T. Moriya and S. Ehara, Ultramicroscopy 42–44 (1992) 744.
[39] T. Oshio, Y. Sakai and S. Ehara, J. Vac. Sci. Technol. B 12 (1994) 2055.
[40] R.L. Smith, W. Lu and G.S. Rohrer, Surf. Sci. 322 (1995) 293.
[41] J. Tersoff and D.R. Hamman, Phys. Rev. B 31 (1985) 805.
[42] S.N. Magonov and M.-H. Whangbo, Adv. Mater. 6 (1994) 335.
[43] S.N. Magonov and M.-H. Whangbo, Surface Analysis with STM and AFM (VCH, Weinheim, 1996).
[44] M.-H. Whangbo and R. Hoffmann, J. Am. Chem. Soc. 100 (1978) 6093.
[45] In this paper, we index V_2O_5 using the conventional setting for space group 59, Pmmn. some authors choose to index the V_2O_5 cell in an alternate setting where the b and c axes are interchanged.
[46] A. Bystrom, K.-A. Wilhelmi and O. Brotzen, Acta Chem. Scand. 4 (1950) 1119.
[47] K.-A. Wilhelmi, K. Waltersson and L. Kihlborg, Acta Chem. Scand. 25 (1971) 2675.
[48] J.Y. Kempf, B. Silvi, A. Dietrich, C.R.A. Catlow and B. Maigret, Chem. Mater. 5 (1993) 641.
[49] K. Nagasawa, Y. Bando and T. Takada, J. Cryst. Growth 17 (1972) 143.